Electronic Supplementary Information for

Boron complexes of aromatic 5-substitued iminopyrrolyl ligands: synthesis, structure, and luminescent properties

Ana I. Rodrigues,[a] Cláudia A. Figueira,[a] Clara S. B. Gomes,[a] D. Suresh,[a,f] Bruno Ferreira,[a] Roberto E. Di Paolo,[a] Daniel de Sa Pereira,[b] Fernando B. Dias,[b] Maria José Calhorda,[c] Jorge Morgado,[d,e] António L. Maçanita,[a] Pedro T. Gomes*[a]

[a] *Centro de Química Estrutural, Departamento de Engenharia Química, Instituto Superior Técnico, Universidade de Lisboa, Av. Rovisco Pais, 1049-001 Lisboa, Portugal.*

[b] *Department of Physics, Durham University, South Road, Durham DH1 3LE, U.K.*

[c] *Centro de Química e Bioquímica and BioISI -Biosystems & Integrative Sciences Institute, Departamento de Química e Bioquímica, Faculdade de Ciências, Universidade de Lisboa, Campo Grande, Ed. C8, 1749-016 Lisboa, Portugal.*

[d] *Instituto de Telecomunicações, Av. Rovisco Pais, 1049-001 Lisboa, Portugal.*

[e] *Department of Bioengineering, Instituto Superior Técnico, Universidade de Lisboa, Av. Rovisco Pais, 1049-001 Lisboa, Portugal.*

[f] *School of Chemical and Biotechnology, SASTRA University, Thanjavur – 613 401, India*

* Corresponding author: Pedro T. Gomes; E-mail: pedro.t.gomes@tecnico.ulisboa.pt

Table of Contents

Isolation of B-N adduct **8b** 2
^{1}H and ^{13}C NMR spectra of complexes **7**-**10** 3
Crystallographic and molecular structure data of boron complexes **8**, **9** and **8b** 7
Computational Studies 10
Cyclic Voltammograms of Complexes **7**–**10** 17
Electroluminescence studies 20

Isolation of B-N adduct 8b

The iminopyrrolyl-BPh_2 compounds **7**-**10** have been prepared in a straightforward manner, following the procedure described in the main text of this article. However,–in one of the preparations carried out in this work for compound **8**, a Lewis acid-Lewis base adduct **8b** (Scheme S1) between the ligand precursor 5-phenyl-2-(*N*-2,6-diisopropylphenylformimino) pyrrole (**4**) with $B(C_6H_5)_3$, was formed instead. Crystals suitable for X-ray diffraction enabled the determination of the molecular structure of **8b** (Scheme S1 and Figure S10).

While in **8** the iminopyrrolyl ligand is chelated to the boron atom through the two nitrogen atoms, forming the usual five-membered ring, in the case of **8b** (Scheme S1), the $B(C_6H_5)_3$ Lewis acid only establishes a coordinative bond between boron and the iminic nitrogen of **4**. The elimination of benzene did not occur in this case, possibly because the ligand precursor *Z* conformation was *syn* instead of the more thermodynamically stable *E* (*anti*).[1] This could result via the unlikely direct formation of the *Z* isomer of ligand precursor **4** (Scheme S1), via umbrella inversion of the planar iminic nitrogen, in the particular (uncontrolled) experimental conditions used in its synthetic condensation reaction. Alternatively, isomerization of the more thermodynamically favoured isomer *E* to *Z* could occur in the presence of BPh_3, since it is known in the literature[2,3] that *E*-aldimines can isomerize to their corresponding Z-aldimines in the presence of boranes. The formation of the *Z* isomer in the adduct, along with the presence of a very bulky 2,6-diisopropylphenyl group, will likely lock the iminopyrrole ring, preventing its rotation about the imino group and the approach of the NH proton to the boron centre, and thus the elimination of benzene.

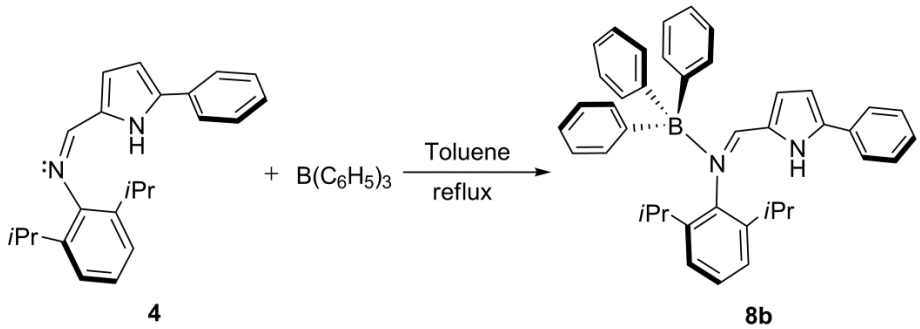

Scheme S1. Synthesis of 5-phenyl-iminopyrrolyl adduct **8b**.

[1] J. Bjorgo, D. R. Boyd, C. G. Watson, W. B. Jennings and D. M. Jerina, *J. Chem.Soc. Perkin II*, 1974, 1081-1084.
[2] K. Huang, S. A. Couchman, D. J. D. Wilson, J. L. Dutton and C. D. Martin, *Inorg. Chem.* 2015, **54**, 8957−8968.
[3] C. Fan, L. G. Mercier, W. E. Piers, H. M. Tuononen and M. Parvez, *J. Am. Chem. Soc.* 2010, **132**, 9604–9606.

^{1}H and ^{13}C NMR spectra of complexes 7-10

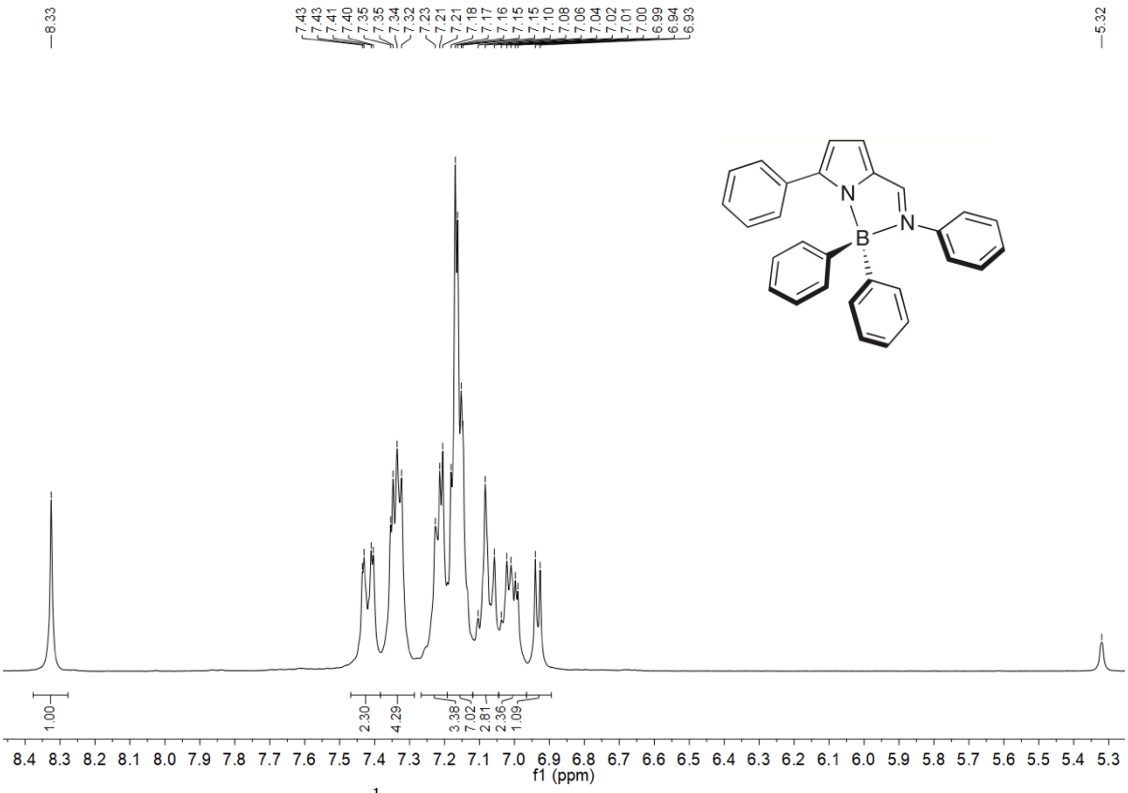

Figure S1. ^{1}H NMR spectrum (300 MHz, CD_2Cl_2) of **7**.

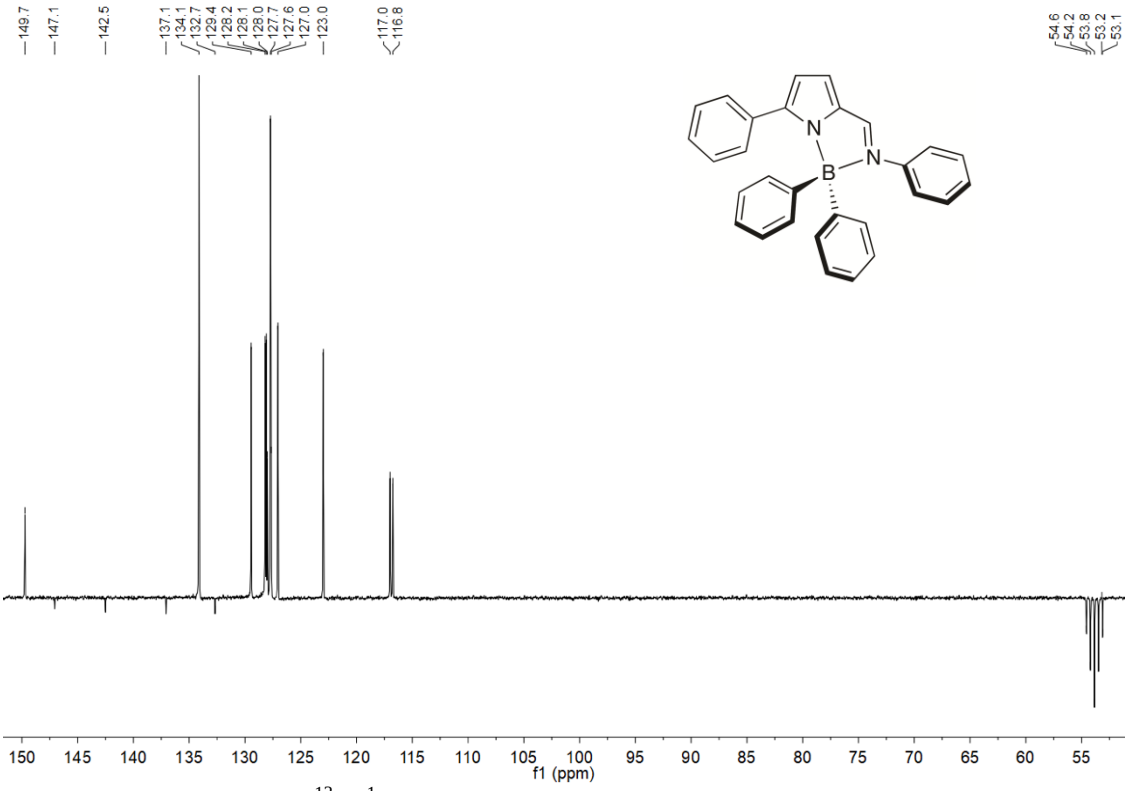

Figure S2. ^{13}C{^{1}H} APT NMR spectrum (75 MHz, CD_2Cl_2) of **7**.

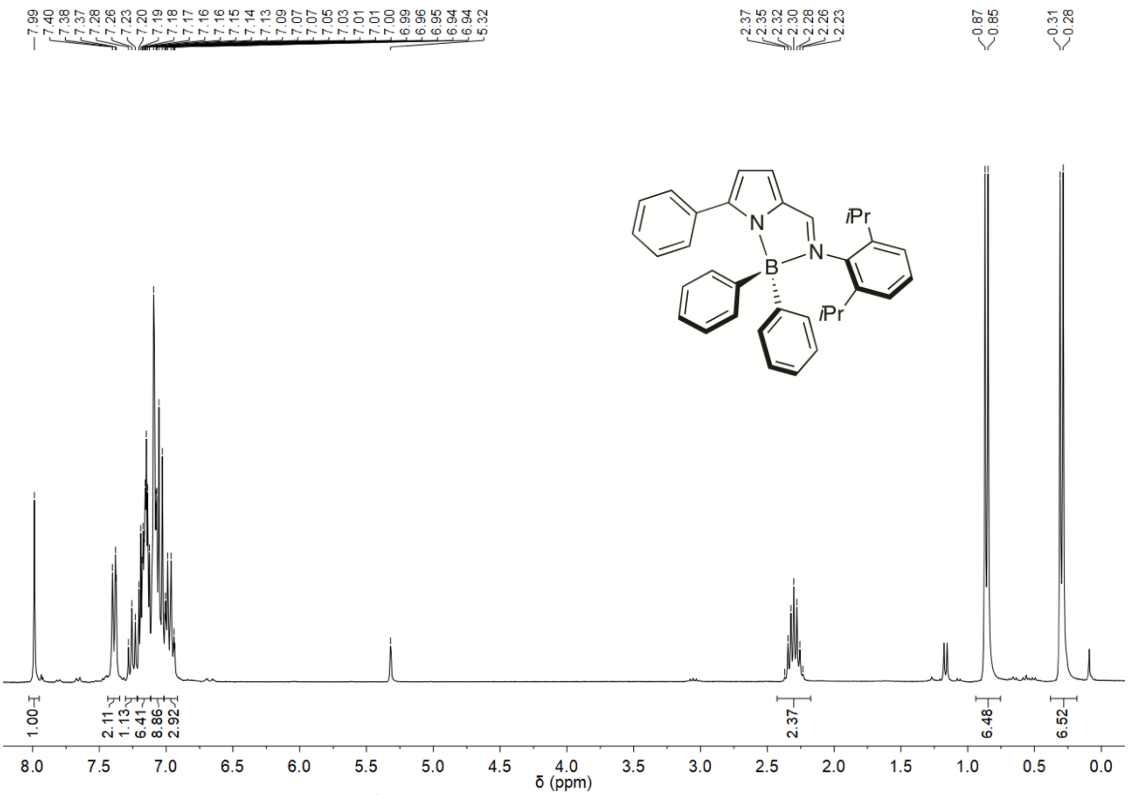

Figure S3. ^{1}H NMR spectrum (300 MHz, CD_2Cl_2) of **8**.

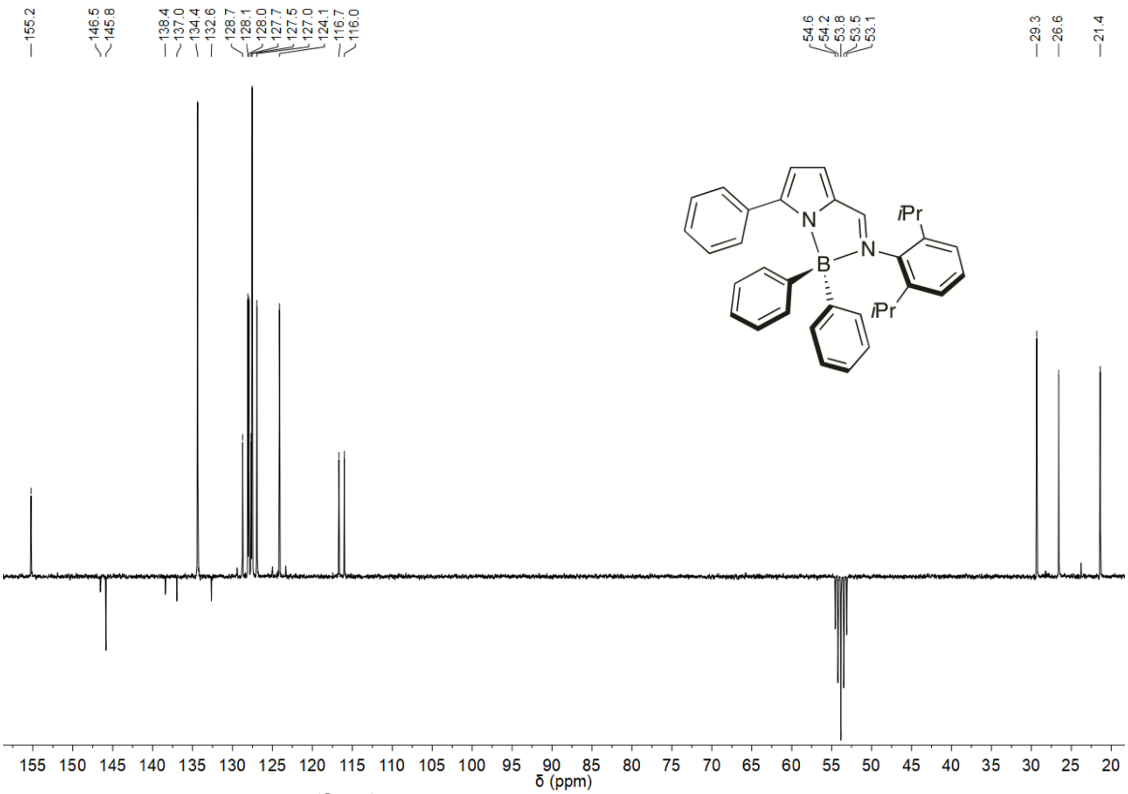

Figure S4. ^{13}C{^{1}H} APT NMR spectrum (75 MHz, CD_2Cl_2) of **8**.

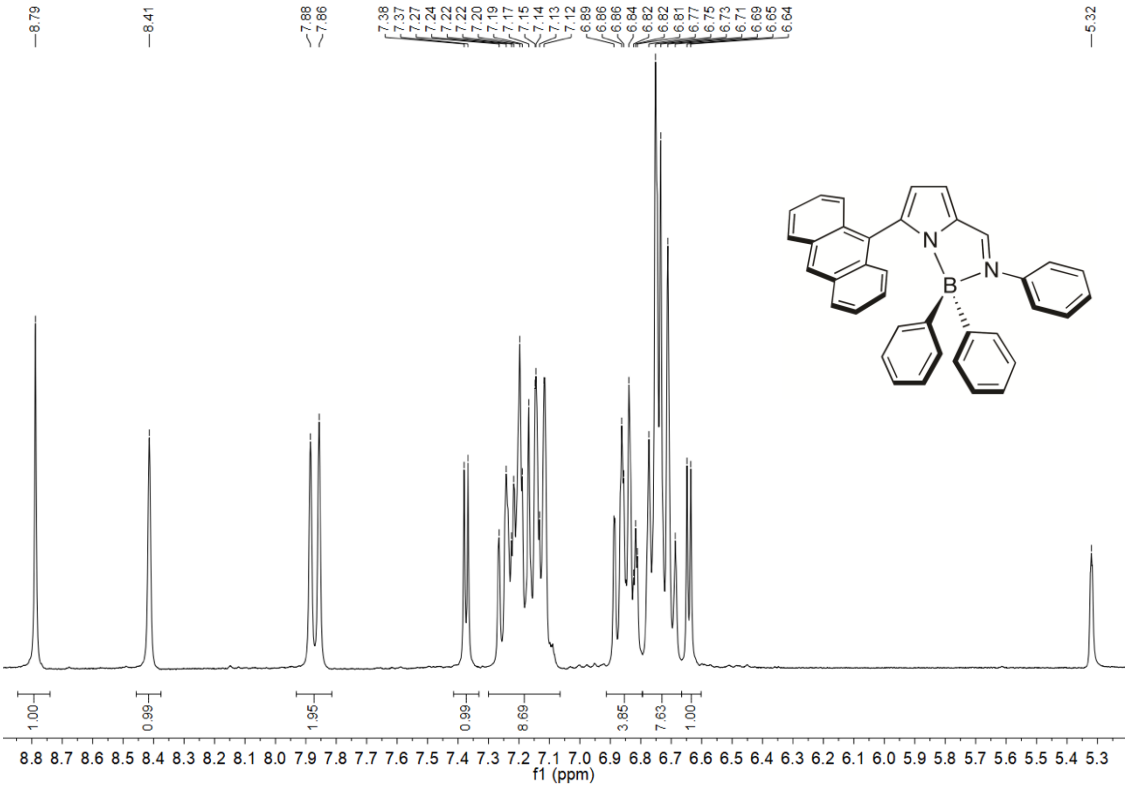

Figure S5. ^{1}H NMR spectrum (300 MHz, CD_2Cl_2) of **9**.

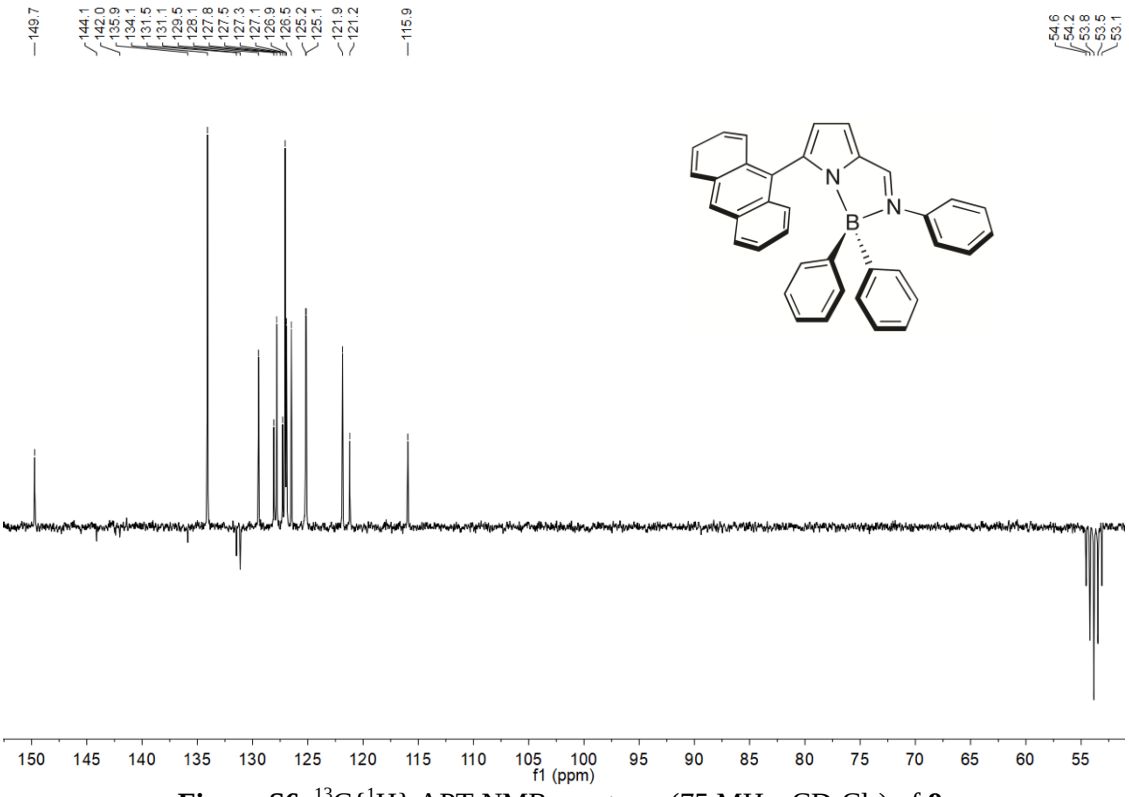

Figure S6. ^{13}C{^{1}H} APT NMR spectrum (75 MHz, CD_2Cl_2) of **9**.

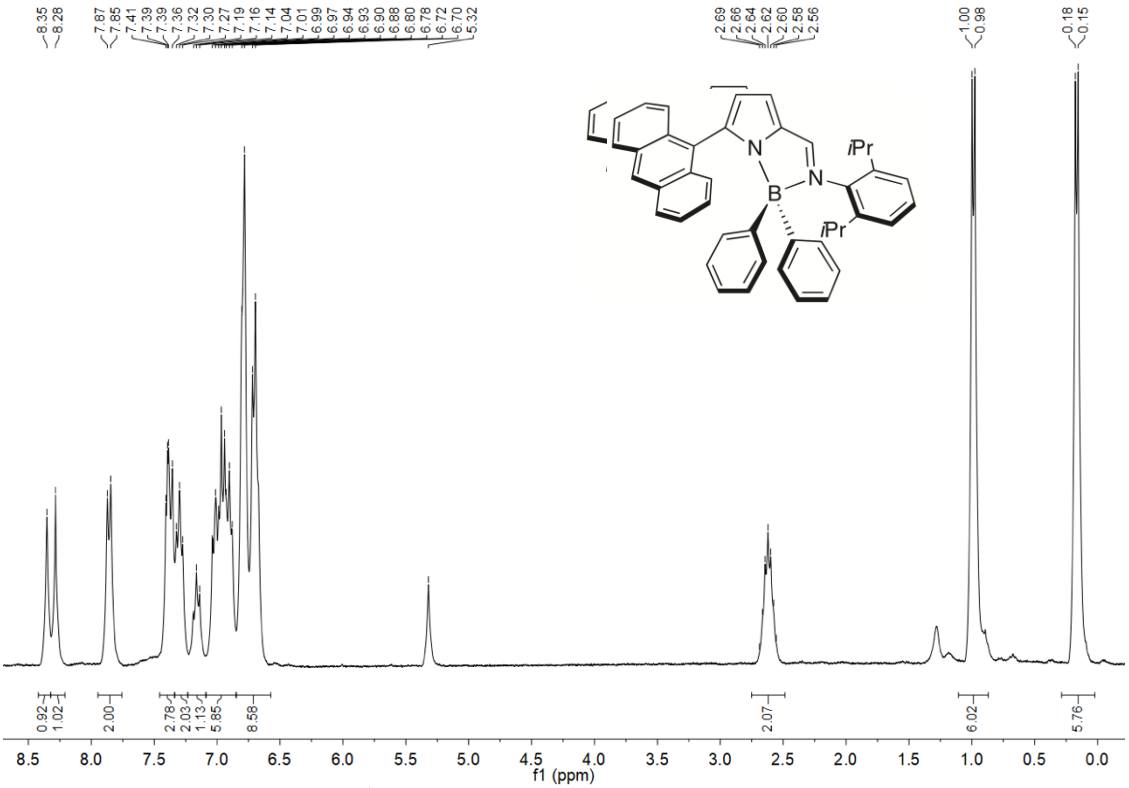

Figure S7. ^{1}H NMR spectrum (300 MHz, CD_2Cl_2) of **10**.

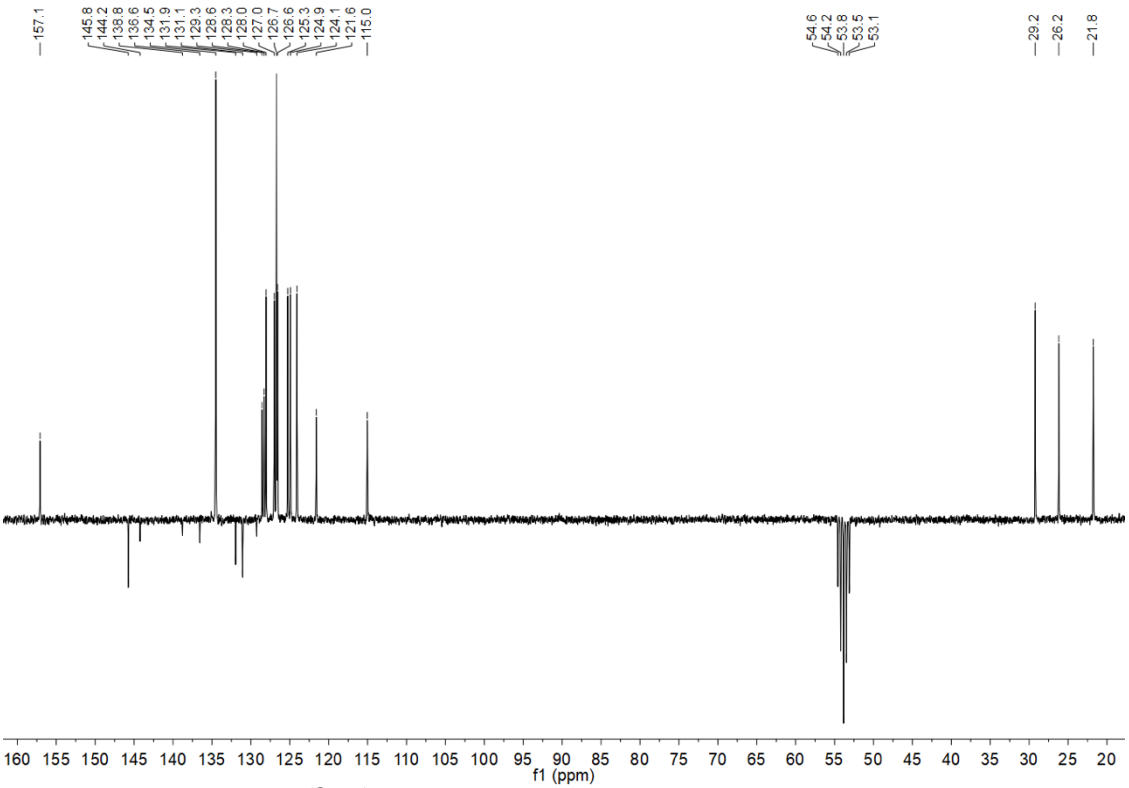

Figure S8. ^{13}C{^{1}H} APT NMR spectrum (75 MHz, CD_2Cl_2) of **10**.

Crystallographic and molecular structure data of boron complexes 8, 9 and 8b

Table S1. Crystallographic data for boron complexes **8**, **9**, and **8b**.

	8	**9**	**8b**
formula	$C_{35}H_{35}BN_2$	$C_{37}H_{27}BN_2$	$C_{41}H_{41}BN_2$, 0.5 (C_6H_{14})
M / g mol^{-1}	494.46	510.41	615.65
λ /Å	0.71073	0.71073	0.71073
T / K	150(2)	150(2)	150(2)
crystal system	Triclinic	Monoclinic	Monoclinic
space group	*P* -1	*P* 21/*n*	*P 21/c*
a / Å	8.7182(8)	12.435(3)	11.832(2)
b / Å	17.212(2)	15.353(4)	14.352(3)
c / Å	18.794(2)	13.984(3)	21.983(4)
α / deg	95.340(4)	90	90
β / deg	99.889(4)	91.186(9)	103.421(7)
γ / deg	90.231(4)	90	90
V / Å^3	2765.6(6)	2669.1(11)	3630.9(12)
Z	4	4	4
ρ_{calc} /g cm^{-3}	1.188	1.270	1.126
crystal size / mm	0.250×0.130×0.130	0.100×0.100×0.060	0.400×0.200×0.100
θ_{max} / deg	25.680	25.681	25.729
total data	21135	21817	23155
unique data	10449	5055	6914
R_{int}	0.1030	0.0878	0.1724
R [I > 2σ(I)]	0.0730	0.0972	0.0780
wR	0.1222	0.2728	0.1532
goodness of fit	0.882	1.034	0.826
ρ min, ρ max	-0.302, 0.281	-0.287, 0.369	-0.237, 0.237

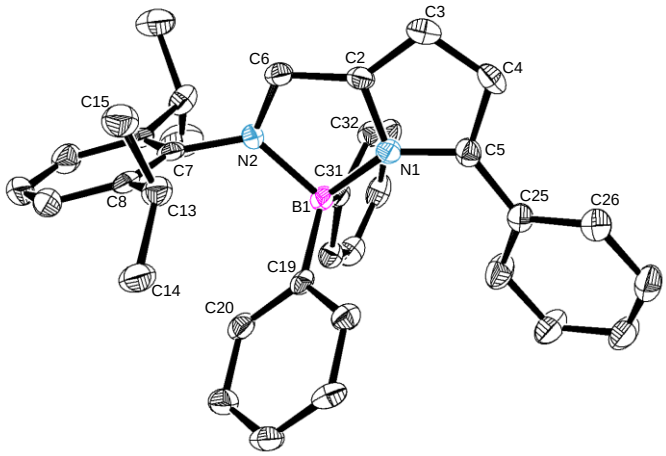

(a)

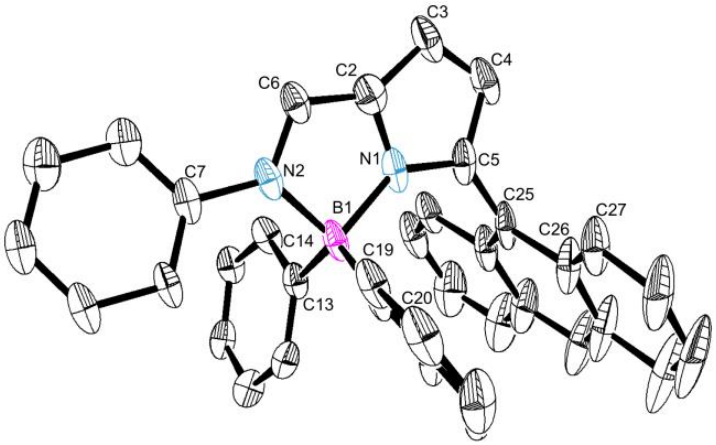

(b)

Figure S9. Perspective views of molecular structures of (a) **8** (molecule A) and (b) **9**. The calculated hydrogen atoms were omitted for clarity and the ellipsoids were drawn at the 50% and 20% probability level, respectively. Compound **8** (molecule A): selected bond distances (Å): N1A-C2A, 1.391(4); N1A-C5A, 1.357(4); N1A-B1A, 1.584(4); N2A-C6A, 1.301(4); N2A-C7A, 1.446(4); N2A-B1A, 1.640(4); C25A-C5A, 1.471(4); C14A-C13A, 1.508(5); C15A-C13A, 1.536(4); C13A-C8A, 1.510(5); C31A-B1A, 1.612(5); C19A-B1A, 1.608(5). Selected bond angles (°): C5A-N1A-C2A, 107.8(3); C2A-N1A-B1A, 110.6(2); C5A-N1A-B1A, 140.9(3); C6A-N2A-C7A, 122.4(3); C6A-N2A-B1A, 110.8(3); C7A-N2A-B1A, 125.8(2); C25A-B1A-N2A, 109.6(3); C19A-B1A-C31A, 117.2(3); N1A-B1A-N2A, 95.3(2); N1A-B1A-C31A, 108.6(3); C20A-C19A-B1A, 122.2(2); C32A-C31A-B1A, 123.7(3); C26A-C25A-C5A, 119.2(3); C4A-C5A-C25A, 126.3(3). Compound **9**: selected bond distances (Å): N1-C2, 1.394(7); N1-C5, 1.342(6); N1-B1, 1.593(7); N2-C6, 1.314(6); N2-C7, 1.412(6); N2-B1, 1.627(8); C5-C25, 1.473(9); C25-C26, 1.442(9); C27-C26, 1.406(7); C13-B1, 1.594(8); C19-B1, 1.622(7); selected bond angles (°): C5-N1-C2, 108.5(5); C2-N1-B1, 112.3(5); C5-N1-B1, 139.0(6); N1-B1-N2, 93.7(4); C6-N2-C7, 123.3(5); C6-N2-B1, 111.1(4); C7-N2-B1, 125.3(4); C20-C19-B1, 121.0(5); C14-C13-B1, 119.9(5); C26-C25-C5, 121.7(5).

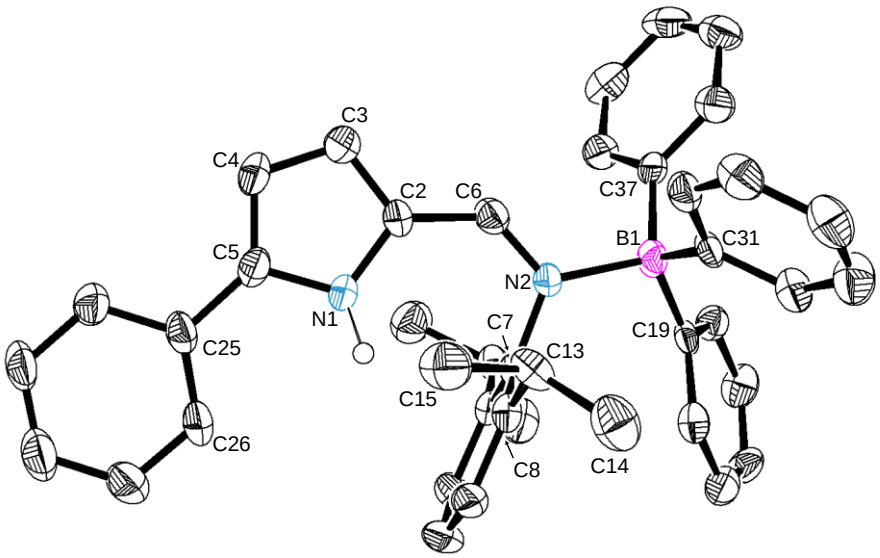

Figure S10. Perspective view of molecular structure of **8b**. The calculated hydrogen atoms were omitted for clarity and the ellipsoids were drawn at the 50% probability level. Selected bond distances (Å): N1-C5, 1.372(5); N1-C2, 1.383(5); N2-C6, 1.304(4); N2-B1, 1.676(5); N2-C7, 1.461(4); C5-C25, 1.452(5); C37-B1, 1.623(6); C19-B1, 1.640(6); C31-B1, 1.638(6); selected bond angles (°): N1-C2-C6, 127.8(4); N2-C6-C2, 130.5(4); C6-N2-B1, 121.0(3); N1-C5-C25, 121.9(3); C19-B1-N2, 107.9(3); C37-B1-N2, 108.0(3); C31-B1-N2, 106.8(3); C6-N2-C7, 116.9(3); C7-N2-B1, 122.1(3).

Compound **8b** was characterised by X-ray diffraction. The B-N bond distance of 1.679(5) and the B-C bond distances of 1.641(6), 1.611(6) and 1.627(6) in **8b** are comparable with those in **8** and **9**. In **8b**, the phenyl ring at the position 5 is virtually coplanar with the 2-iminopyrrole fragment, displaying a very small N1-C5-C25-C26 dihedral angle (-3.7(6)º), whereas the dihedral angle of this fragment with the bulky *N*-2,6-$iPr_2C_6H_3$ group (C6-N2-C7-C8) is 85.1(4)º.

Computational Studies

Table S2. Calculated (DFT) dihedral angles (°) for complexes **7**–**12** in the ground and first singlet excited state using different methods.

Cmpd	Ground state					First singlet excited state				
	BP86 (GP)	PBE0 (A)	B3LYP (B)	PBE0D (A/D3)	B3LYPD (B/D3)	BP86 (GP)	PBE0 (A)	B3LYP (B)	PBE0D (A/D3)	B3LYPD (B/D3)
Dihedral ∠	C6-N2-C7-C8									
7	42	43	48	48	49	14	14	14	13	12
8	75	75	74	76	77	63	58	58	59	60
9	27	29	30	19	18	-16	-9	7	5	5
10	77	77	77	77	77	76	73	79	72	70
11	29	35	36	36	38	2	3	5	2	4
12	74	71	72	72	73	42	45	71	46	73
Dihedral ∠	N1-C5-C25-C26									
7	-28	-28	-31	-26	-32	19	17	18	16	17
8	-26	-18	-26	-15	-25	0	3	3	3	3
9	-86	-87	-92	-99	-98	-50	-56	-119	-129	-125
10	74	100	99	99	99	128	128	126	126	125

Table S3. Calculated HOMOs and LUMOS energies (eV) for complexes **7**–**12** using different methods.

Cmpd	GP		THF		CH_2Cl_2		A		A/D3		B		B/D3	
	HOMO	LUMO	HOMO	LUMO	HOMO	LUMO	HOMO	LUMO	HOMO	LUMO	HOMO	LUMO	HOMO	LUMO
7	-5.258	-3.000	-5.277	-2.899	-5.273	-2.949	-6.032	-2.140	-6.030	-2.119	-5.747	-2.147	-5.747	-2.141
8	-5.303	-2.912	-5.278	-2.835	-5.324	-2.912	-6.079	-2.099	-6.070	-2.102	-5.784	-2.110	-5.776	-2.112
9	-5.034	-3.057	-5.038	-2.872	-5.118	-2.961	-5.835	-2.168	-5.783	-2.228	-5.535	-2.168	-5.484	-2.271
10	-5.060	-2.896	-5.048	-2.846	-5.131	-2.894	-5.849	-2.108	-5.828	-2.088	-5.542	-2.102	-5.504	-2.087
11	-5.396	-2.933	-5.414	-2.877	-5.511	-2.978	-6.346	-2.122	-6.336	-2.096	-6.037	-2.165	-6.028	-2.137
12	-5.502	-2.700	-5.548	-2.699	-5.652	-2.805	-6.514	-1.949	-6.517	-1.951	-6.197	-2.009	-6.203	-2.013

Table S4. Absorption wavelength (λ), energy (E), composition, oscillator strength (O.S.) of the most intense TDDFT electronic transitions, and absorption wavelength maxima calculated for complexes **7-10** (GP), compared with experimental solution absorption maxima (λ_{max}).

Transition	λ (nm)	E (eV)	Composition	O.S.	λ_{max} (calc) (nm)	λ_{max} (exp) (nm)
Cmpd 7						
1	434	2.85	H→L (69%), H-1→L (25%)	0.307		
2	415	2.99	H-1→L (51%), H-2→L (39%), H→L (9%)	0.066	431	416
3	410	3.03	H-2→L (56%), H-1→L (22%), H→L (16%)	0.115		
Cmpd 8						
1	415	2.98	H→L (62%), H-2→L (22%), H→L (11%)	0.198		
2	402	3.08	H-1→L (81%)	0.029	411	394
3	388	3.19	H-2→L (82%)	0.127		
Cmpd 9						
1	438	2.83	H→L+1 (73%), H-1→L+1 (13%)	0.101	438	
2	389	3.18	H-6→L (47%), H-1→L (24%), H-7→L (20%),	0.140	386	412
3	385	3.22	H-2→L (82%)	0.220		
Cmpd 10						
1	451	2.75	H→L+1 (48%), H-1→L+1 (22%), H-1→L (15%), H→L (12%)	0.063	450	
2	352	3.52	H-9→L (28%), H-7→L+1 (20%), H→L+2 (18%), H-1→L (12%)	0.070		392
3	346	3.59	H→L+3 (27%), H-8→L+1 (21%), H-7→L+1 (13%), H-1→L (11%)	0.051	345	
4	341	3.64	H→L+4 (36%), H-1→L (13%), H-8→L+1 (12%)	0.067		

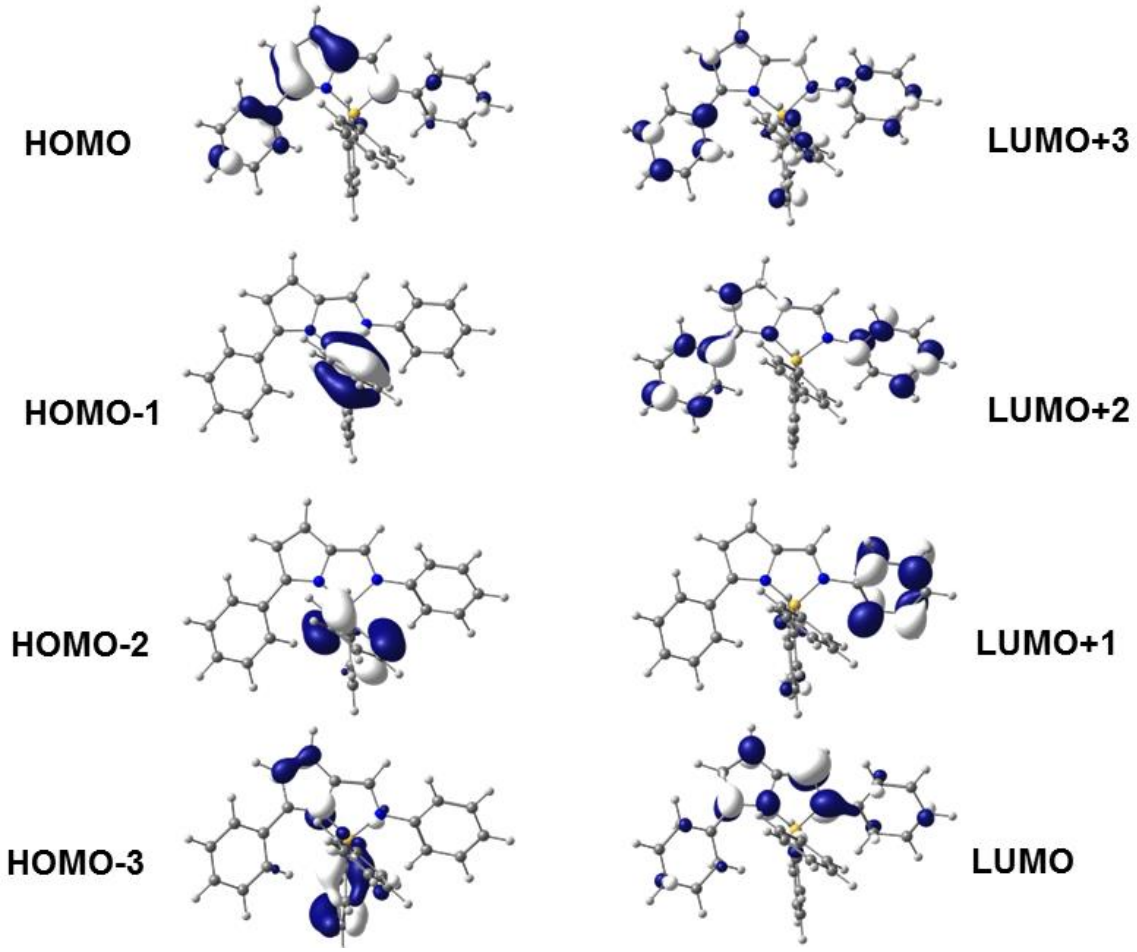

Figure S11. Frontier orbitals of complex **7**.

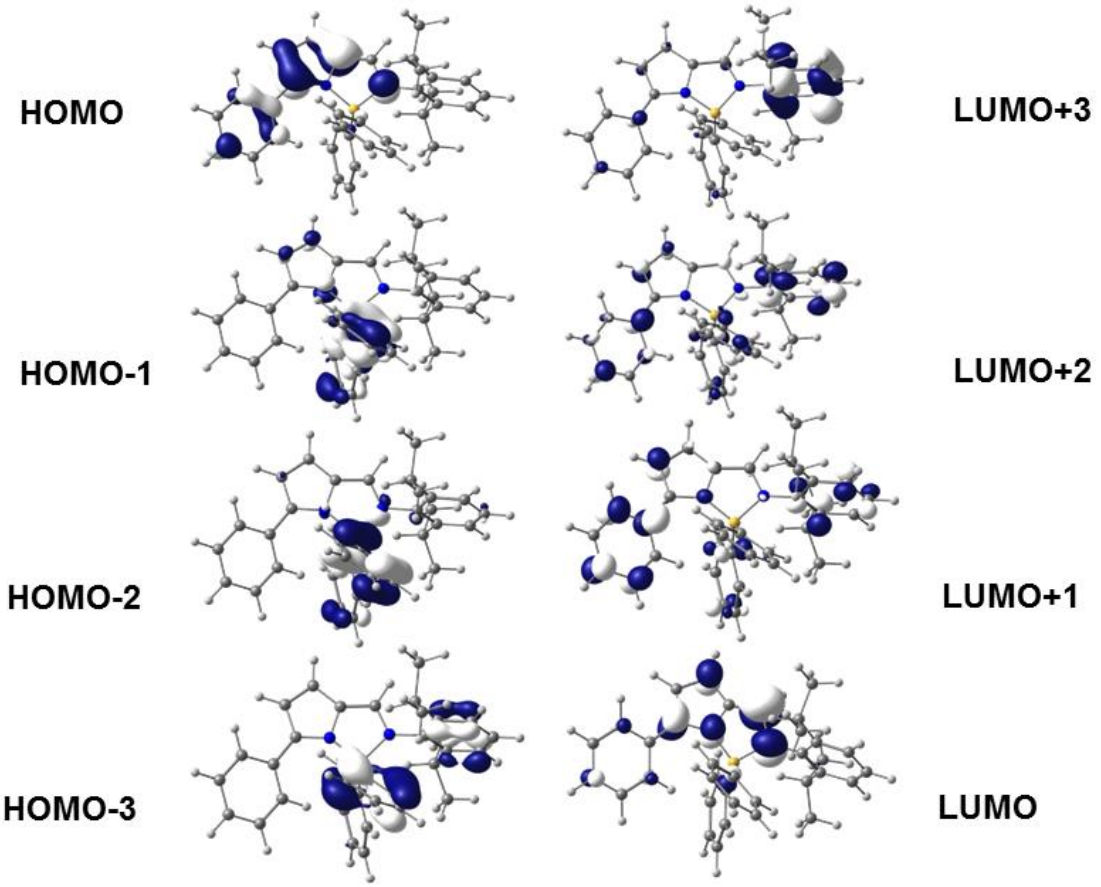

Figure S12. Frontier orbitals of complex **8**.

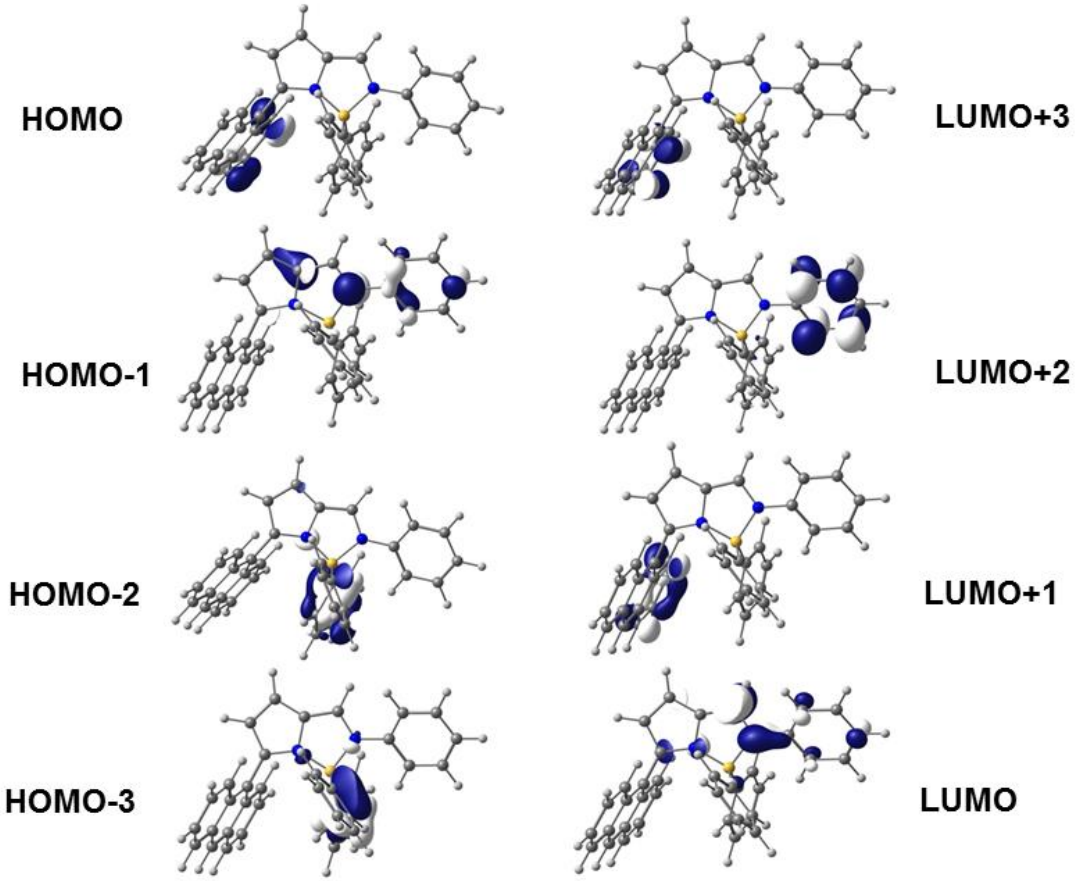

Figure S13. Frontier orbitals of complex **9**.

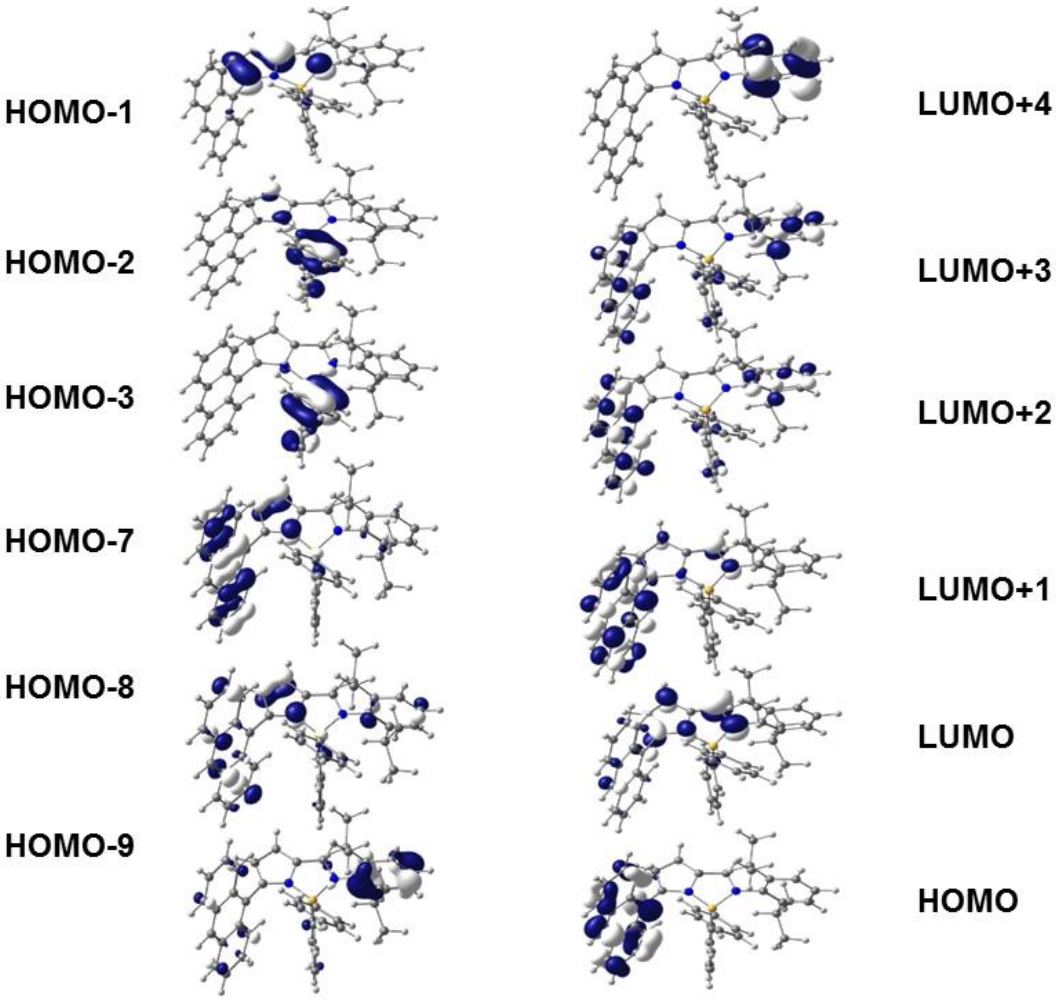

Figure S14. Frontier orbitals of complex **10**.

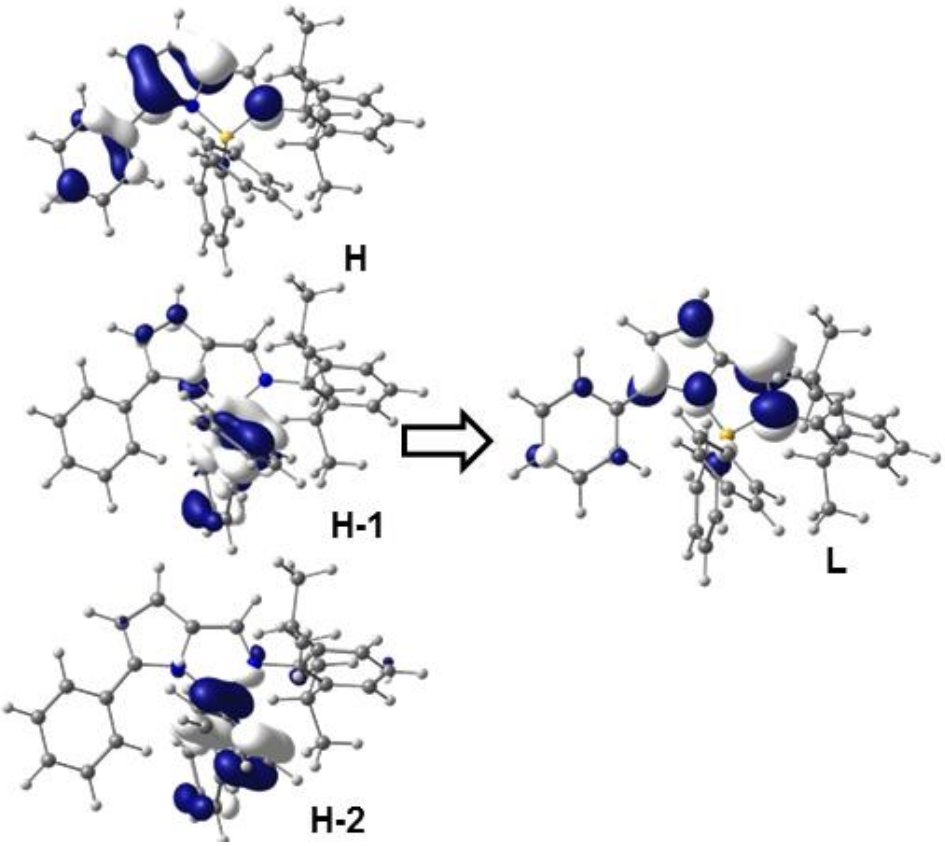

Figure S15. Representation of the orbitals involved in the lowest energy transition (GP) of complex **8**.

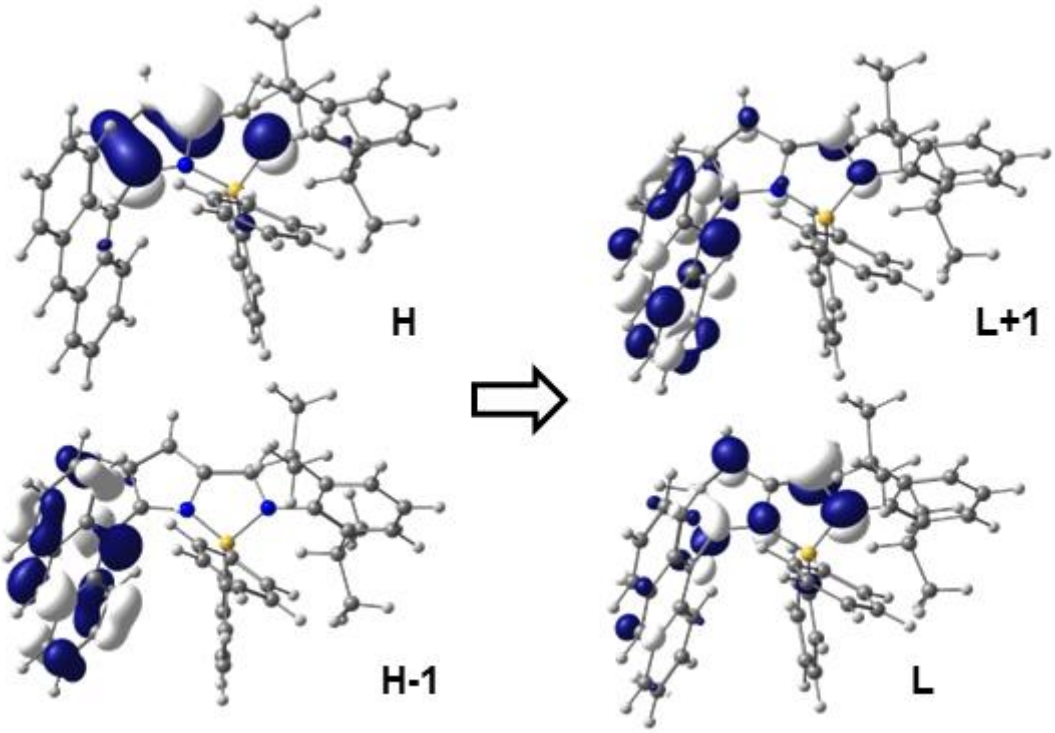

Figure S16. Representation of the orbitals involved in the lowest energy transition (GP) of complex **10**.

Cyclic Voltammograms of Complexes 7–10

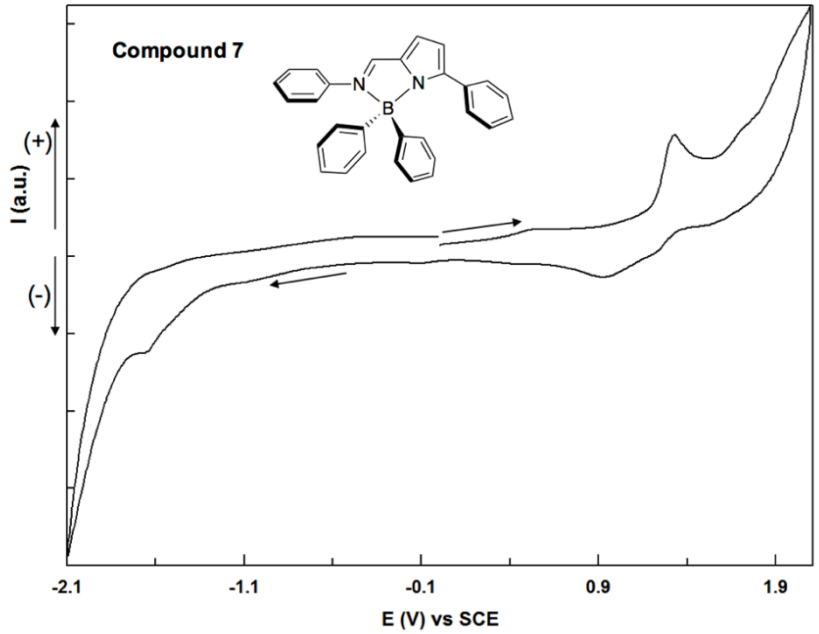

Fig. S17. Cyclic voltammogram obtained for compound **7** at a scan rate of 50 mV/s *versus* SCE (Saturated Calomel Electrode) as the reference electrode. The SCE was calibrated against Fc/Fc^{+} redox couple, for which the measured half-wave potential ($E_{Fc/Fc+}$) was 4.27 eV.

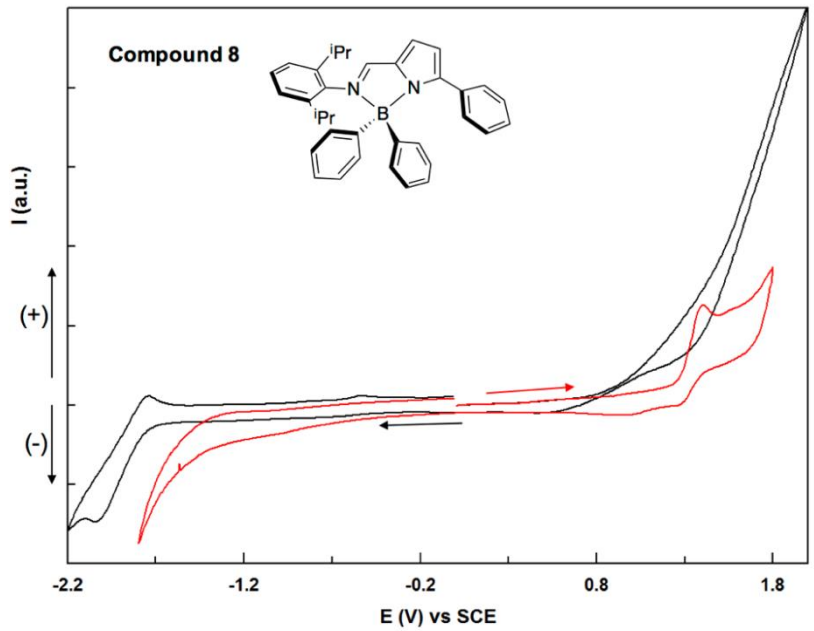

Figure S18. Cyclic voltammogram obtained for compound **8** at a scan rate of 50 mV/s *versus* SCE, as the reference electrode, calibrated against Fc/Fc^{+} redox couple. The measured half-wave potential ($E_{Fc/Fc+}$) was 4.27 and 4.13 eV.

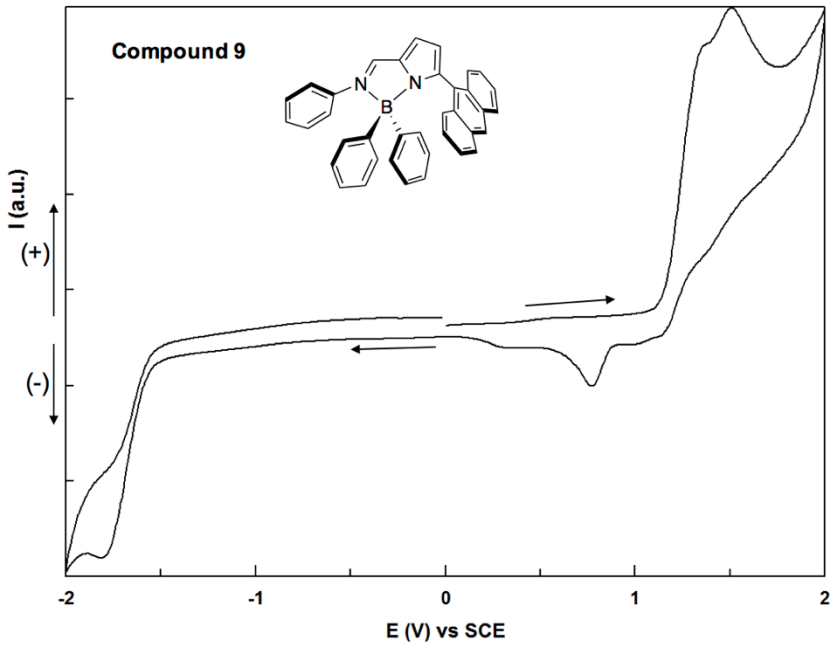

Fig. S19. Cyclic voltammogram obtained for compound **9** at a scan rate of 50 mV/s *versus* SCE, as the reference electrode, calibrated against Fc/Fc^{+} redox couple. The measured half-wave potential ($E_{Fc/Fc+}$) was 4.26 eV.

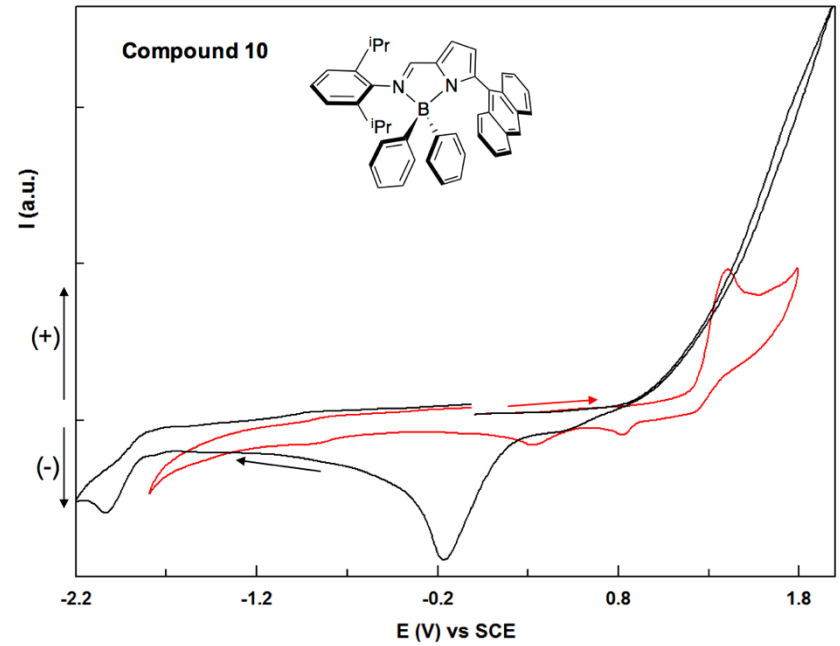

Fig. S20. Cyclic voltammogram obtained for compound **10** at a scan rate of 50 mV/s *versus* SCE, as the reference electrode, calibrated against Fc/Fc^{+} redox couple. The measured half-wave potential ($E_{Fc/Fc+}$) was 4.24 and 4.15 eV.

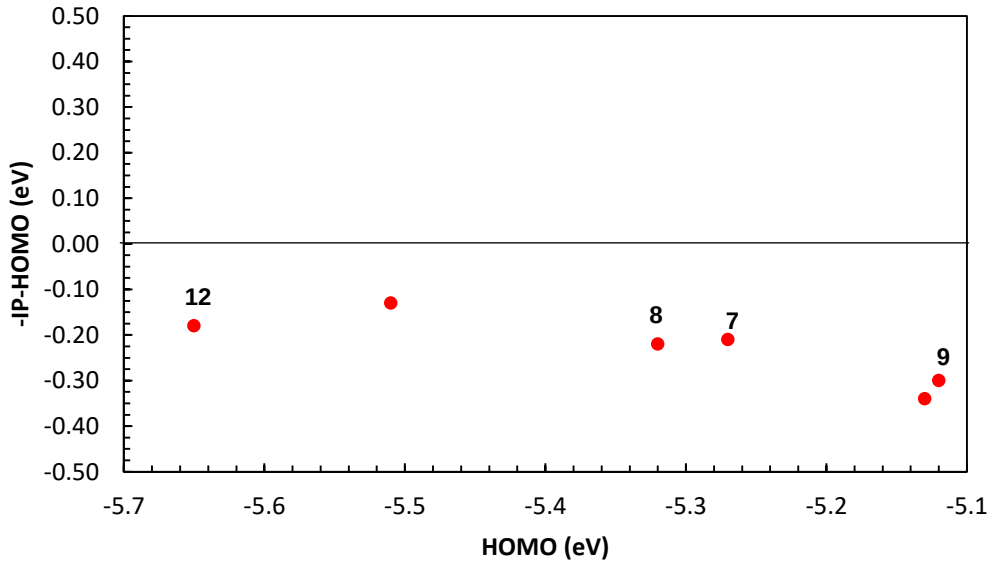

(a)

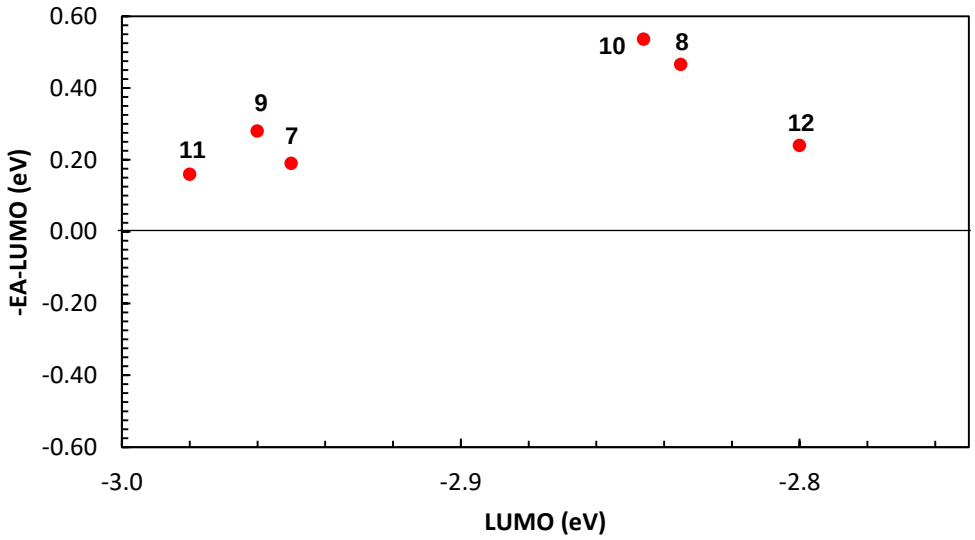

(b)

Fig. S21. Plots of (a) the difference between –IP and HOMO versus the energies of the HOMOs, and of (b) the difference between –EA and LUMO versus the energies of the LUMOs of compounds **7**–**12**. IP and EA were estimated from cyclic voltammetry measurements, and the energies of the HOMOs and LUMOs were determined by DFT (CH_2Cl_2) and, in the particular case of the LUMOs of compounds **8** and **10**, by DFT (THF).

Electroluminescence studies

A preliminary characterization of the electroluminescent properties was made using neat films of the synthesized molecules **7**-**10** as emissive layers (Table S5), in two different device structures. The first type was prepared using vacuum thermal deposition, with the following structure: ITO/PEDOT:PSS/Cmpd/Ca/Al. The second type of devices was fabricated by a wet process (spin-coating technique), using an additional hole-transporting/electron-blocking layer of poly(bis-4-butylphenyl-*N*,*N*-bisphenyl)benzidine (polyTPD)) (*ca.* 10 nm). ITO (indium-tin oxide) was used as the anode, PEDOT:PSS (poly(3,4-ethylenedioxythiophene):poly(styrenesulfonate)) (*ca.* 40 nm) as the hole injection layer, calcium (1.5 nm) as cathode protected by an overlayer of aluminium (*ca.* 80 nm). The emissive layer (Cmpd) thickness was within the range 100-110 nm.

Table S5. Characteristics of OLEDs based on complexes **7**-**12** including maximum luminance (L_{max}, $cd.m^{-2}$, and voltages at which the maximum value is obtained), external quantum efficiency (EQE_{max}, %, and voltages at which the maximum value is obtained), current efficiency ($\eta_{L_{max}}$, $cd.A^{-1}$), and Commission Internationale de l'Éclairage (CIE) colour coordinates.

Cmpd no.	ITO/PEDOT:PSS/Cmpd/Ca/Al				ITO/PEDOT:PSS/PolyTPD/Cmpd/Ca/Al			
	L_{max}	EQE_{max}	$\eta_{L_{max}}$	CIE	L_{max}	EQE_{max}	$\eta_{L_{max}}$	CIE
7	4.3 (@10V)	2.2×10^{-3} (@9V)	6.7×10^{-3}	0.25, 0.53	301 (@11.5V)	0.03 (@10.5V)	0.08	0.25, 0.53
8	161 (@14V)	0.02 (@14V)	0.04	0.20, 0.26	2716 (@11.5V)	0.15 (@11.5V)	0.31	0.22, 0.25
9	1450 (@12.5V)	0.06 (@10V)	0.23	0.31, 0.61	4140 (@11.5V)	0.07 (@10.5V)	0.26	0.31, 0.61
10	150 (@23.5V)	0.05 (@22.5V)	0.16	0.37, 0.56	129 (@18V)	0.02 (@16V)	0.08	0.33, 0.56
11[a]	0.35	1.5×10^{-4}	3.8×10^{-4}	0.37, 0.53	[b]	[b]	[b]	[b]
12[a]	0.09	1.9×10^{-6}	3.6×10^{-6}	[b]	[b]	[b]	[b]	[b]

[a] Values from Ref. 5f, with OLED structure: ITO/PEDOT:PSS/Cmpd/Ca/Al (spin-coating); [b] Not available.

Table S5 shows that most of the molecules displayed better results when applied as emissive layers in the second type of organic light-emitting diodes, containing the additional polyTPD hole-transporting layer. In fact, the first devices fabricated with compounds **7**-**9** exhibited luminance maxima within the range 4.3-1450 $cd.m^{-2}$, together with external quantum efficiencies maxima up to 0.06 %. Typically, the maximum luminance is recorded before the device breaks down. These results show that the devices based on **7**-**9** performed better than those from **11** and **12**. These outcomes were enhanced upon insertion of a polyTPD hole-transporting/electron-blocking layer, which is expected to improve

the selective holes migration to the emissive layer, while confining the electrons, and, consequently, increase recombination efficiency. Thus, it was possible to achieve luminance maxima from 301 up to 4140 cd m^{-2} along with external quantum efficiencies maxima of 0.03-0.15 %. However, the opposite result was observed with 2-iminopyrrolyl boron complex **10**, which displayed a better performance in the first type of device. Nevertheless, this molecule exhibited poor device characteristics in both cases (Table S5, Figures S23-S24).

The boron complex **8** also gives good results when applied as neat emissive layer in OLEDs containing a polyTPD hole-transporting layer. In fact, the maximum luminance is higher than that of the OLEDs based on the other two analogues **7** and **10**. The electroluminescence (EL) spectrum of **8**, exhibits a second band between 550 and 700 nm that is not present in neither the solution nor film photoluminescence, which affects the device performance, being possibly related to a degradation process (Figure S22). Supporting evidence for such degradation comes from the fact that when the devices are driven near the limit (maximum voltages) its intensity is increased in an irreversible way.

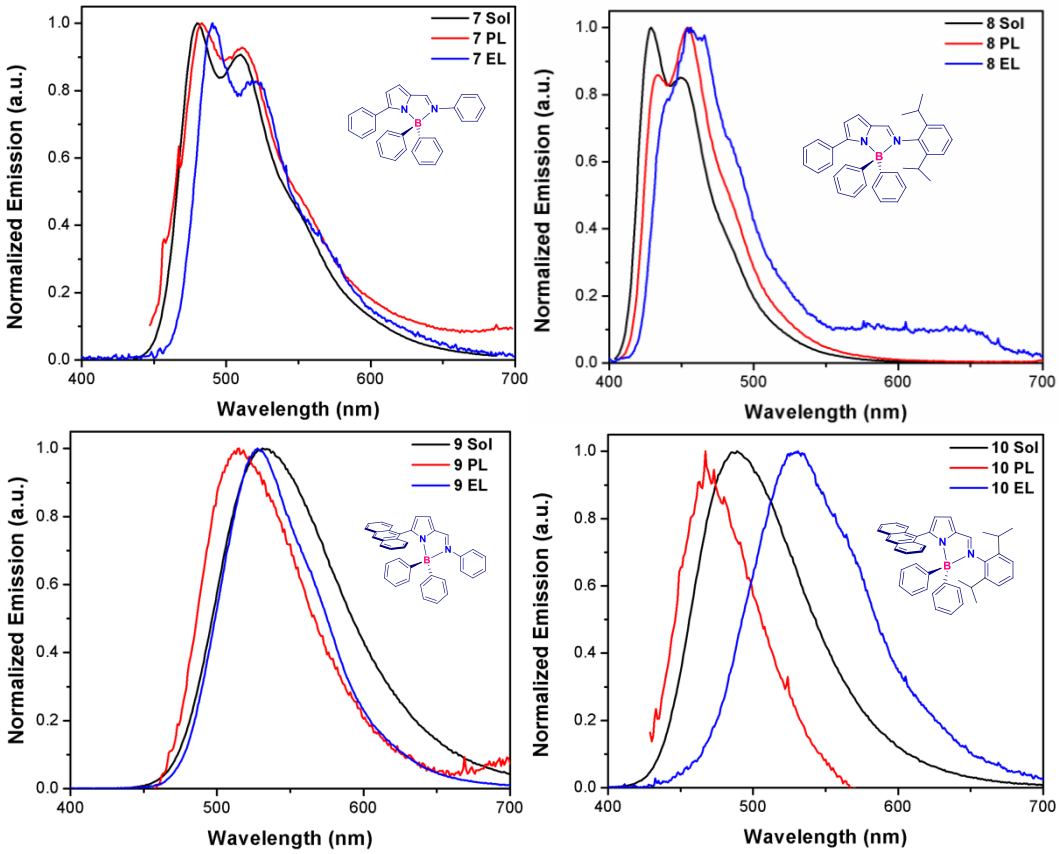

Figure S22. Electroluminescence spectra (EL) of OLED devices containing compounds **7**-**10** as emitters compared to film photoluminescence (PL) and solution fluorescence spectra in THF (Sol).

The recorded EL spectra of compounds **7**, **9** and **10** are also compared with solution fluorescence and film photoluminescence spectra in Figure S22. Compounds **7** and **9** exhibit similar spectra shape and wavelength maxima, proving the inexistence of aggregates formation or degradation processes.

Regarding complex **10**, a red-shifted EL spectrum (531 nm) was obtained in relation to its film PL (470 nm) and solution (489 nm) spectra. Such red-shifted spectrum is common to both device types tested and may indicate that the emissive state generated upon electrical excitation is different from that generated upon photoexcitation. We also find that the electroluminescence spectrum of compound **10** when driven at high voltage, near the limiting value before device break down, is irreversibly modified, indicating degradation. No similar observations were made for either compound **7** or **9**. Further studies are required to clarify the origin of such shift.

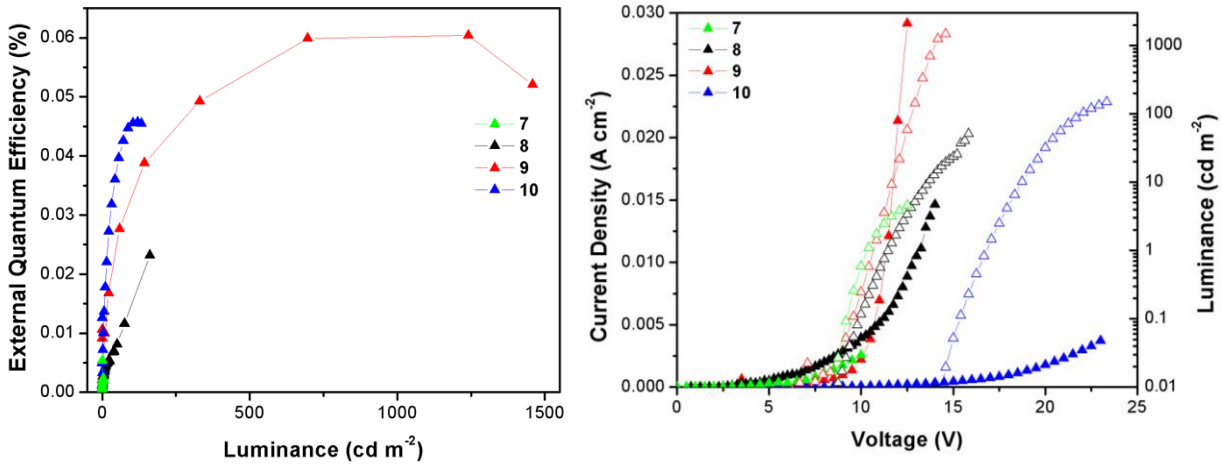

(a) (b)

Figure S23. Characteristics of the first type of OLED devices (ITO/PEDOT:PSS/Cmpd/Ca/Al) using compounds **7**-**10** as emitters: (a) External Quantum Efficiency (EQE) vs. Luminance; (b) Current Density (filled symbols)/Luminance (open symbols).

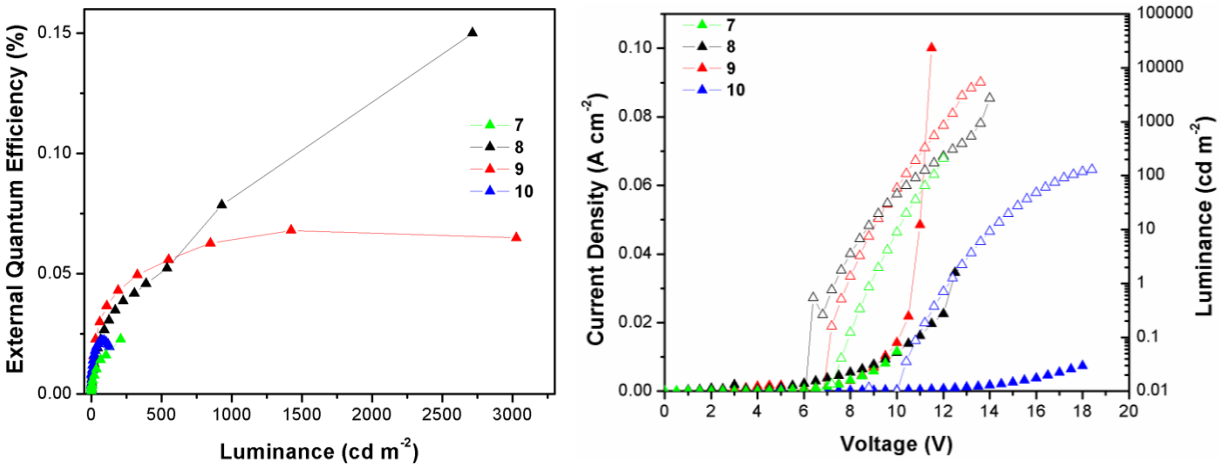

(a) (b)

Figure S24. Characteristics of the second type of OLED devices (ITO/PEDOT:PSS/polyTPD/Cmpd/Ca/Al) using compounds **7**-**10** as emitters: (a) External Quantum Efficiency (EQE) vs. Luminance; (b) Current Density (filled symbols)/Luminance (open symbols) vs. Voltage.